ACS APPLIED MATERIALS & INTERFACES

www.acsami.org

Research Article

# Potential-Dependent ATR-SEIRAS and EQCM-D Analysis of Interphase Formation in Zinc Battery Electrolytes

Katherine Betts, Yuhan Jiang, Michael Frailey, Kidus Yohannes, and Zhange Feng*

Cite This: https://doi.org/10.1021/acsami.4c15318

Read Online

ACCESS | Metrics & More | Article Recommendations | Supporting Information

**ABSTRACT:** With the heightening interest in bivalent battery technology, there arises a necessity for a thorough investigation into zinc-ion battery (ZIB) electrolytes, accommodating their chemical attributes and potential-dependent structural dynamics. While the phenomenon of in situ solid electrolyte interphase formation is extensively documented in lithium-ion batteries, its analogous occurrences in ZIBs remain limited. Herein is a comparative study of three zinc electrolytes of interest: $ZnSO_4$, ZnOTF, and $Zn(TFSI)_2$/LiTFSI hybrid water-in-salt electrolyte. Additionally, the impact of an acetonitrile additive is scrutinized, with a comparative assessment of the interfacial behavior in aqueous solutions. Utilizing ATR-SEIRAS, potential-dependent alterations in the composition of the electrolyte/electrode interface were monitored, while EQCM-D facilitated a comprehensive understanding of variations in the mass and structural properties of the adsorbed layer. Aqueous $ZnSO_4$ demonstrated the accumulation of porous $Zn_4SO_4(OH)_6{\cdot}xH_2O$ at negative potentials, leading to a mass of 1.47 $\mu$g cm$^{-2}$ after five cycles. Bisulfate formation was observed at positive potentials. SEIRAS measurements for ZnOTF demonstrated reorientation and surface adsorption of $CF_3SO_3^-$ to favor $CF_3$ at the surface for positive potentials, and acetonitrile showed increased stability for the electrode at negative potentials. The additive was also reported to lead to the accumulation of a substantial passivation layer with viscoelastic properties. The zinc water-in-salt showed exceptional surface stability at negative potentials and a widened potential window. A thin rigid zinc SEI layer is reported with a mass of 0.7 $\mu$g cm$^{-2}$. The compositional intricacies of these surface structures are discussed in relation to their solvent conditions. This investigation not only sheds light on the initial charge/discharge cycles in ZIBs but also underscores their pivotal role in instigating enduring transformations that can significantly influence their long-term cycling performance.

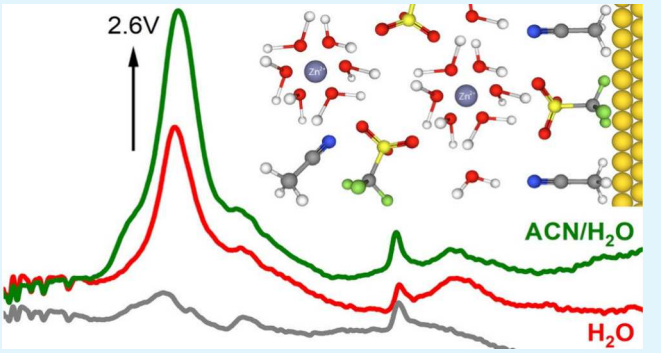


**KEYWORDS:** *Zinc battery electrolytes, electrode interface, SEI, SEIRAS, EQCM*

## 1. INTRODUCTION

The technological advancements of modern society, coupled with global population growth, have led to an escalating demand for energy production and storage solutions. Concerns about global warming and the environmental impacts of traditional energy sources have significantly heightened interest in renewable energy conversion, however, the transition to renewable energy presents several challenges. Current battery systems provide environmental benefits only after several hundred cycles due to the substantial energy costs associated with their manufacturing processes.[1] The rapid expansion of the electric vehicle (EV) and photovoltaic markets has further exacerbated concerns about the supply of lithium and cobalt, which are predominantly used in lithium-ion batteries. There is therefore a growing interest in alternatives that are more abundant and cost-effective. Among these, multivalent metals, such as those used in zinc-ion batteries (ZIBs), offer the advantages of high energy density and improved safety.[2]

ZIBs have garnered considerable attention due to zinc's high capacity density, nontoxicity, and enhanced eco-efficiency compared to other alternatives.[3] Nonetheless, the development of ZIBs faces significant challenges, including the need for improved cathode materials capable of efficiently capturing zinc ions, and the advancement of electrolyte systems that enhance performance while minimizing parasitic side reactions and zinc dendrite growth.[4] Optimization of the electrode/electrolyte interface, and the development of novel separator treatments,[5,6] are crucial for overcoming the detrimental effect of dendrite growth and "dead" zinc at the interface. There is substantial interest in utilizing solid-electrolyte interphase

Received: September 8, 2024
Revised: October 29, 2024
Accepted: October 30, 2024

(SEI) to regulate the deposition of zinc in ZIBs. SEI layers, typically associated with lithium-ion batteries (LIBs), can be applied artificially by coating the anode with metal−organic frameworks (MOFs) or formed *in situ* with the use of electrolyte additives.[7] Surface studies of the electrode/electrode interface offer invaluable insight into the formation and benefits of SEI layers for ZIB technology and beyond. Although this study focuses on aqueous and water-in-salt zinc electrolytes for traditional ZIBs, the techniques and findings aim to inform other alternative battery technologies such as metal-air batteries, other multivalent electrolytes e.g. magnesium, aluminum salts, and direct alternatives to lithium such as sodium-ion batteries.

Three zinc salts were selected for this study: $ZnSO_4$, $Zn(CF_3SO_3)_2$ (also known as ZnOTF), and $Zn(TFSI)_2$/LiTFSI hybrid water-in-salt electrolyte. Aqueous zinc sulfate, an affordable and commonly used compound in the study of zinc-based electrochemistry, serves as a baseline for observing surface deposition and hydrogen evolution. ZnOTF, being soluble in acetonitrile, allows for comparative experiments in both water and a 1:1 H2O:ACN solvent mixture. Lastly, the more expensive and recently explored acetonitrile−water-in-salt (AWIS) zinc electrolyte has attracted significant interest due to its widened potential window, enhanced cycling capabilities, and suppressed dendrite growth. Gaining insights into the mechanisms underlying these improved electrode/electrolyte interfaces is crucial for the design of future ZIBs, and for developing viable long-term solutions for clean, high-capacity energy storage.

Acetonitrile (ACN) is a promising additive for ZIBs, which could enhance charge transfer and reduce both hydrogen evolution and dendrite growth.[8] Understanding the mechanism by which acetonitrile enhances performance is essential, particularly given the discrepancies in the reported solvation behavior and surface adsorption of acetonitrile molecules. Another aim of this study is to deepen the understanding of the mechanisms by which acetonitrile facilitates charge transfer at the electrode surface while protecting against corrosion and dendrite growth.

## 2. THEORETICAL CONSIDERATIONS

**ATR-SEIRAS.** Surface-enhanced infrared absorption spectroscopy (SEIRAS) has demonstrated significant growth and development since the 1990s, particularly following the introduction of attenuated total reflectance (ATR) methods by Osawa, which have enabled detailed studies of thin film electrode/electrolyte interfaces.[9] The enhancement of the infrared response in SEIRAS arises from both electromagnetic and chemical effects, primarily due to plasmon resonance with metal particles on the surface. Additionally, the vibronic coupling of chemisorbed species at the surface contributes to this enhancement.[10] These surface-bonded ions can exhibit increased dipole moments and enhanced spectral peaks, presenting unique opportunities for investigating the solid-electrolyte interphase (SEI). SEIRAS enhancement diminishes rapidly with distance from the surface, being effective up to ∼10 nm.[11] Given that a typical SEI layer is 10−50 nm thick, the initial stages of SEI formation should be observable using SEIRAS techniques. Previous studies on lithium-ion batteries have predominantly utilized surface-enhanced Raman spectroscopy (SERS); however, optimized SEIRAS techniques offer superior signal-to-noise ratios and sensitivities.[12]

There are various instrumental methods for ATR-SEIRAS, each offering distinct advantages. Silicon hemispheres and ZnSe prisms are commonly used as internal reflection elements (IREs) for ATR-SEIRAS, though specialized microgrooved silicon wafers have demonstrated greater transparency at long mid-IR wavelengths (<1400 $cm^{-1}$).[13] With many electrolyte systems relying on the analysis of S−O and C−F bonds, this region is particularly important to our research. By employing a cooled mercury cadmium telluride (MCT) detector, we can optimize the sensitivity of our observations in this region.

**Stark Effect and Coverage.** Potential-dependent spectral measurements present unique challenges. Applying potential to the electrode/electrolyte interface can induce a blue shift in spectral peaks; for instance, the $SO_4$/Au interface can exhibit shifts exceeding 70 $cm^{-1}/V$.[14] There are two main contributions to this shift. The first is the vibrational Stark effect (VSE), which describes how a molecule's vibrational energy levels shift due to the applied potential. Molecules in excited vibrational states have different dipole moments, leading to the shifting, splitting, and/or broadening of infrared spectral peaks.[15] The second contribution to spectral shifts is coverage-dependent, arising from the coupling and lateral repulsion between adsorbed ions on the surface. Dipolar interactions and their proximity to the surface can cause peak splitting or redistribution of intensities.[16] Both the Stark effect and coverage dependence contribute to the spectral shift simultaneously; however, their relative impact depends on the specific system and whether the surface has reached maximum coverage. For example, Pfisterer et al. investigated the adsorption of sulfate on gold surfaces and found that the Stark effect accounted for approximately 80% of the shift, while interactions between sulfate ions due to coverage contributed about 20% of the total shift.[17]

**Acetonitrile Electrolyte Additive.** Acetonitrile and other additives such as N,N-dimethylformamide (DMF) have drawn attention as additives to aid in reducing hydrogen evolution and encourage even distribution of zinc deposition in ZIBs.[18] In aqueous systems with ACN, adsorption sites are predominantly occupied by adsorbed acetonitrile, thereby reducing parasitic reactions. Ilic et al. reported that even in a mixed solvent with 10% ACN and 90% water, the surface exhibited a preferential affinity for ACN over water.[19] The competition among the adsorption of ACN, water, and anions has been previously explored, revealing that ACN dominates surface adsorption until very high or low potentials are reached. This dominance slightly hinders anion adsorption, as evidenced by the associated current, but also decreases problematic hydrogen adsorption.[20] Acetonitrile as an additive has been shown to shift the onset of hydrogen evolution reaction (HER) further from the potential of zinc plating.[19] Decreased HER disturbance and electrode corrosion are both benefits of replacing water at the electrode surface. Adsorbed acetonitrile has also been shown to distribute charge more evenly at the surface, shielding the electrode from dendrite growth.[21]

Faguy et al. proposed a model for acetonitrile/water electrolyte systems that explains ACN adsorption due to positive charge in two ways.[22] Some ACN molecules orient perpendicularly to the electrode surface, while others form hydrogen bonds with chemisorbed water at the interface. These ACN-$H_2O$ hydrogen-bonded species can be identified by a blue shift of approximately 10 $cm^{-1}$, often resulting in an


https://doi.org/10.1021/acsami.4c15318
ACS Appl. Mater. Interfaces XXXX, XXX, XXX−XXX

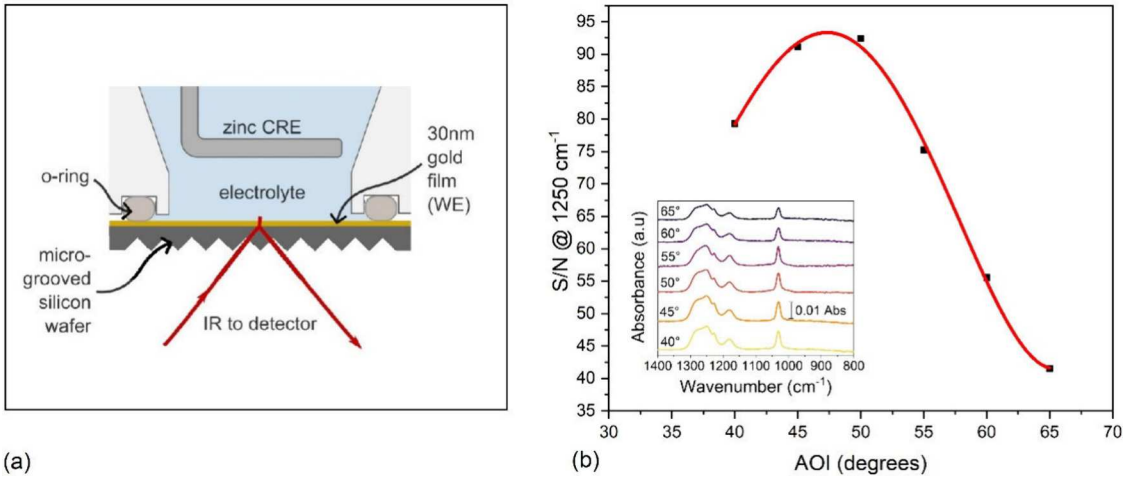


**Figure 1.** (a) Instrumental schematic for SEIRAS spectro-electrochemical cell. (b) Signal-to-noise comparison for 1m aqueous ZnOTF electrolyte with varying angles of incidence for the spectro-electrochemical cell. S/N ratio compared at the $SO_3$ peak at 1030 cm$^{-1}$.

asymmetric shouldered peak where these two species overlap.[23]

For ACN directly at the surface, a perpendicular orientation is predominant, with the nitrogen end of the ion facing the surface at positive potentials and the $CH_3$ end facing the surface at negative potentials. Although there has been some suggestion that ACN adopts a CN $\eta^2$ configuration, with both carbon and nitrogen atoms bonded parallel to the metal, spectroscopic studies have shown this to be unlikely for the ACN/Au interface. This conclusion is based on the reported intensity ratios of the C ≡ N peaks to the $CH_3$ peaks.[24] Density functional theory (DFT) modeling indicates that the $\eta^2$ configuration is more probable for Pt surfaces, showing a preference for 'bent' parallel adsorption around the potential of zero charge (PZC).[25] There is consensus that positive potentials result in perpendicular chemisorption with the nitrogen end, while models suggest that negative potentials lead to 'free' ACN, with the $CH_3$ end oriented perpendicularly but without chemisorption.[26]

**Rigid Films, Viscoelasticity, And Porosity.** Although the red/blue shift of spectral peaks can provide insights into the adsorption and coverage at the interface, it does not yield information about the physical properties of the layer itself. By using electrochemical quartz crystal microbalance with dissipation monitoring (EQCM-D), we can observe film deposition on the electrode surface in relation to the applied potential and assess changes in the viscoelasticity and porosity of the developing solid-electrolyte interphase (SEI) layer. EQCM-D measurements utilize the resonant frequency of an oscillating piezoelectric quartz crystal sensor. When mass is deposited, the damping of the oscillation causes a shift in the resonant frequency, a relationship described by the Sauerbrey equation (1959):[27]

$$\Delta m = -C\Delta f_n/n \quad (1)$$

where $\Delta m$ is the change in mass at the surface, $\Delta f_n/n$ is the change in resonant frequency for overtone $n$, and $C$ is the mass sensitivity constant associated with the QCM crystal. This relationship remains sound for thin rigid films, however when a soft elastic layer or a rigid porous layer is deposited, energy loss during oscillation deviates from Sauerbrey behavior, leading to reduced $\Delta f_n/n$ measurements and calculated mass.[28]

Viscoelastic and porous properties can be confirmed by observing increased changes in dissipation during the deposition of a surface film. If the ratio between changes in dissipation and frequency is large, the film is no longer considered solid rigid. Reviakine et al. set a limit of 0.4 $\mu$Hz for a 5 MHz quartz crystal.[29] If the $\Delta D_n/(\Delta f_n/n)$ ratio is significantly below 0.4 $\mu$Hz, the film is deemed rigid, allowing for reliable mass calculation using the Sauerbrey equation. Another method to identify soft or porous films involves examining the spread of plotted $\Delta D_n$ and $\Delta f_n/n$ measurements across different overtones.[30] Generally, the relationship between three or more overtones and their spread can be utilized in various modeling and fitting techniques to calculate a more accurate mass.[31]

Electrochemical deposition and SEI layers often form porous structures that allow cations to reach the electrode surface. Despite being inherently rigid, these films can behave similarly to viscoelastic systems because porous films dissipate significant crystal quartz oscillation. This dissipation occurs due to the increased strain of the film itself and the movement of liquid within its pores during electrolyte mass transport.[32] Accurate quantitative mass measurements of porous systems would require the implementation of hydrodynamic modeling.[33] However, for the purposes of this study, the Sauerbrey equation is used for mass calculation, in conjunction with dissipation measurements, offering quantitative analysis for rigid layers and qualitative observations for porous/viscoelastic layers.

## 3. EXPERIMENTAL SECTION

**Sample and Instrument Preparation.** The specialized microgrooved SEIRAS wafer was prepared by polishing with 1.0 $\mu$m alumina followed by 0.05 $\mu$m alumina, sonication, and rinsing with ultrapure water (Barnstead, 18.2 MΩ·cm). Cleaned, dry wafers were coated with 30 nm gold film by thermal evaporation (Denton DV-502). Electrolyte solutions were prepared to the required molality (mol/kg) using ultrapure water and acetonitrile (ACN) solvent. Zinc sulfate, $ZnSO_4$ (Spectrum), zinc trifluoromethanesulfonate, ZnOTF (AmBeed) were prepared at 1m. A 5m AWIS electrolyte was then prepared with $Zn(TFSI)_2$ and LiTFSI (1.251g/0.002 mol $Zn(TFSI)_2$, 11.48g/0.04 mol LiTFSI, 2g water, and 6.4 g acetonitrile).[34] 0.3 mL of electrolyte was purged with nitrogen before each measurement. A nitrogen blanket was kept at the surface for the duration of the measurements.


https://doi.org/10.1021/acsami.4c15318
ACS Appl. Mater. Interfaces XXXX, XXX, XXX−XXX

**ATR-SEIRAS Measurements.** Figure 1a illustrates a schematic representation of the SEIRAS cell utilized in this study. Measurements were conducted employing a 30 nm gold film electrode deposited onto a microgrooved specialized silicon wafer. The experimental setup employed a spectro-electrochemical cell (Jackfish Cell, PIKE Technologies) in tandem with a Fourier-transform infrared (FTIR) spectrometer (Nicolet iS50R, Thermo Fisher). The optimal angle of incidence for the spectro-electrochemical cell was determined through a systematic examination of various angles, considering the signal-to-noise ratio (Figure 1b). Background spectra were taken at each angle of incidence and 1m aqueous ZnOTF was added for measurement with 1 V (approximately open circuit potential, OCP) applied. Signal to noise ratio was compared using the signal peak at 1030 $cm^{-1}$. Following this exercise, the ATR-SEIRAS measurements were carried out at an angle of incidence of 50°. The FTIR spectrometer, equipped with a nitrogen-cooled MCT detector, acquired 128 scans at a resolution of 4 $cm^{-1}$ for each measurement. Spectra were obtained incrementally across the potential range from OCP in either negative or positive potential directions and were visually stacked for comparative analysis.

Chronoamperometry protocols were executed employing a zinc counter/reference electrode (CRE) in conjunction with a potentiostat (PGSTAT302N, Metrohm). An identical setup was employed to acquire cyclic voltammograms to determine an appropriate potential window for the ATR-SEIRAS experiments.

**EQCM-D Measurements.** An electrochemical quartz crystal microbalance system with dissipation monitoring (eQCM-I Mini, MicroVacuum Ltd.) was employed in conjunction with an electrochemical cuvette (QSHE-open, MicroVacuum Ltd.). The working electrode (WE) consisted of a gold-coated quartz crystal, while a zinc counter/reference electrode (CRE) was utilized. Electrolytes were subjected to nitrogen purging and blanket during measurements to maintain an inert atmosphere. Cyclic voltammetry experiments were conducted in floating mode using a scan rate of 0.5 mV/s (SP300, Biologic) spanning the range from OCP to the onset of zinc reduction (1−0 V). Simultaneously, EQCM measurements of frequency and dissipation changes were recorded across the fundamental frequency through overtone 9 (i.e., 5 MHz, 15, 25, and 35 MHz) for the 5 MHz crystal. Prior to utilization, quartz crystals were cleaned using piranha solution followed by rinsing with ultrapure water to ensure optimal performance.

## 4. RESULTS AND DISCUSSION

**Cyclic Voltammetry.** Cyclic voltammograms (cycle 1) for all electrolytes are shown in Figure 2. Experiments for $ZnSO_4$ and both ZnOTF electrolytes were taken between −0.3 V to 2.6 V, however, the potential window was extended to −0.4 V for Zn AWIS to reach zinc deposition. $ZnSO_4$ responds with higher zinc deposition/dissolution current due to a smaller potential window compared to the other salts. The CVs for ZnOTF in different solvents show ACN to widen the potential window compared to the purely aqueous solution, and for the AWIS electrolyte it is widened again, with the onset of zinc deposition at −0.25 V, an additional 0.1 V beyond that of the ZnOTF $H_2O$/ACN solution. Similarly, the positive potential was extended by 0.1 V before oxygen evolution at the gold electrode. The wider potential window for WIS electrolytes has been linked to an improved environment of stable O−H bonds, and less "free water" available for degradation at the electrode surface.[35]

Shown in the inset of Figure 2 is the enlarged CV at the oxidative potentials, indicating Au electrode being oxidized at ca. 1.9 V vs $Zn/Zn^{2+}$ reference electrode in all electrolytes. IR spectrum recorded beyond such potential shows the structure of the electrolyte on gold oxide surface instead of metallic gold, and such information facilitate the understanding of electrolyte on the surface of cathode electrodes in ZIBs, e.g., metal oxide.

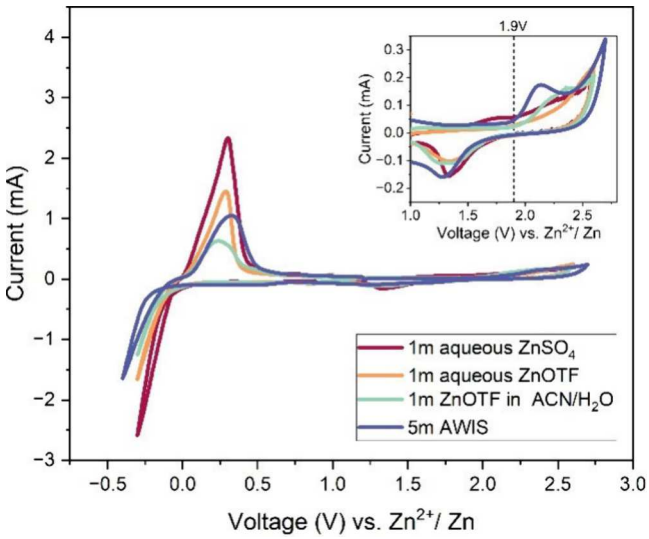


**Figure 2.** Cyclic voltammograms (cycle 1) of Au film electrode collected in the Jackfish cell containing 1 m aqueous $ZnSO_4$ (red), 1 m aqueous ZnOTF (yellow), 1 m ZnOTF in $H_2O$/ACN (green), and 5 m AWIS (blue) at a scan rate of 50 mV/s. Inset: Extract demonstrating the onset of oxidation at ca.1.9 V.

**ATR-SEIRAS Measurements.** Figure 3 illustrates the potential-dependent SEIRAS spectra for $ZnSO_4$ electrolyte. See Table 1 for peak assignments for all electrolytes and associated references. The peak at 967 and 1080 $cm^{-1}$ can be attributed to symmetric ($\nu_s$) and asymmetric ($\nu_{as}$) stretching of the $SO_4^{2-}$ ion, respectively.[36,37] The rapid increased intensity of these peaks at negative potentials from 0.4 V (0.6 V below OCP, 1.0 V) suggests the accumulation of sulfate at the electrode surface. The emergence of a shoulder on the $\nu_{as}$ peak at 1133 $cm^{-1}$ is due to a change in symmetry of the $SO_4^{2-}$ ion, from $T_d$ to $C_{3v}$, often associated with monodentate adsorption.[38,39] The $\nu_s$ peak is unseen before the emergence of the split $\nu_{as}$ peak because of the complete symmetry of the $SO_4^{2-}$ ion (forbidden IR transition). In contrast to these findings, the net negative charge of the sulfate ion and previous models in the literature would suggest there is no increased concentration of $SO_4^{2-}$ within the negative potential range.[40,41] It is anticipated that there will be an augmentation in the presence of water and $Zn^{2+}$, in the form of zincate ($Zn(OH)_4^{2-}$) ions adsorbed at the surface, which can precipitate as ZnO coinciding with zinc reduction.[42] The presence of increased $SO_4^{2-}$ at the surface is however explained by the formation of a $Zn_4SO_4(OH)_6{\cdot}xH_2O$ passivation layer at the electrode surface which is a common corrosion product in zinc electrolytes.[43]

Upon the application of positive potential (Figure 3b), a significant peak at 1235 $cm^{-1}$ is observed from 1.6 V. This peak is a minor feature at OCP and negative potentials yet becomes the most prominent of peaks at positive potentials. This peak is associated with protonated sulfate ions in the form of bisulfate and/or hydrate complexes.[44] Kunimatsu et al. report similar findings for platinum electrodes, showing an increased presence of bisulfate in the oxide region with positive potential.[45] Although there is minimal increase in the scale of the weak broad $\nu_{as}$ peak 1080 $cm^{-1}$, a substantial blue shift of 28 $cm^{-1}$/V is observed from 1080 to 1108 $cm^{-1}$. This indicates the S−O bonds are experiencing the effects of applied potential, due to the vibrational Stark effect (VSE). This


https://doi.org/10.1021/acsami.4c15318
ACS Appl. Mater. Interfaces XXXX, XXX, XXX−XXX

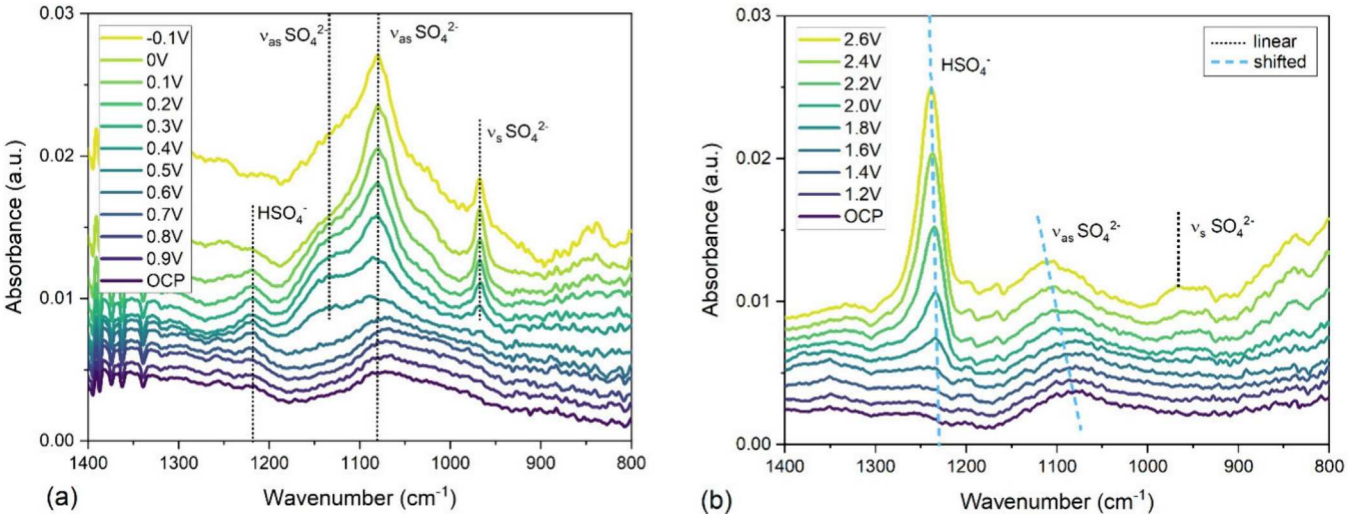


**Figure 3.** Potential dependent ATR-SEIRAS spectra for (a) 1m aqueous $ZnSO_4$ at negative potentials and (b) positive potentials.

**Table 1. Peak Assignments for ATR-SEIRAS Spectra for 1m $ZnSO_4$ (Top), 1m ZnOTF (Middle), 5m AWIS (Bottom)**[a]

| Peak assignment | Wavenumber ($cm^{-1}$) | Refs |
|---|---|---|
| | Zn $SO_4$ | |
| $\nu_s$ $SO_4$ | 967 | 36, 37 |
| $\nu_{as}$ $SO_4$ | 1080, 1133 | 36−39 |
| $\nu_{as}$ $HSO_4$ | 1235 | 44, 45 |
| | Zn OTF | |
| OH | 975 | 53, 54 |
| $\nu_s$ $SO_3$ | 1030 | 46−50 |
| $\nu_{as}$ $CF_3$ | 1175, 1225 | 46−49 |
| $\nu_s$ $CF_3$ | 1255 | 46−49 |
| $\nu_{as}$ $SO_3$ | 1280 | 46−50 |
| | Zn AWIS | |
| $\nu_{as}$ SNS | 1055 | 59, 60 |
| $\nu_s$ $SO_2$ | 1135 | 59, 60 |
| $\nu_{as}$ $CF_3$ | 1188, 1212 | 59, 60 |
| $\nu_s$ $CF_3$ | 1231 | 59, 60 |
| $\nu_{as}$ $SO_2$ | 1322, 1346 | 59, 60 |

[a]Wavenumbers recorded at OCP or potential of peak emergence.

blue shift begins as the adsorbed bisulfate peak emerges at 1235 $cm^{-1}$. Although the broad nature of the $\nu_{as}$ peak is not suggestive of surface adsorption, the dynamic relationship between these two peaks shows the $SO_4^{2-}$ to adsorb at the electrode surface and become protonated. The $\nu_s$ peak of $SO_4^{2-}$ is also weak and broad and can be seen to emerge at potentials above 1.8 V, although any associated blue shift is difficult to determine.

SEIRAS spectra collected toward the negative direction (OCP to 0 V) for aqueous ZnOTF are presented in Figure 4. Within this IR region, the dumbbell shaped $OTF^-$ ion ($CF_3SO_3^-$) can be observed via S−O and C−F vibrational modes. Symmetric stretching for $SO_3$ and $CF_3$ are observed at 1030 and 1255 $cm^{-1}$ respectively.[46−49] Asymmetric stretching of $SO_3$ is observed at 1280 $cm^{-1}$, and is associated with tridentate coordination of the $SO_3$ group with $Zn^{2+}$.[50] The proximity of the $CF_3$ and $SO_3$ vibrational bands causes conflicting allocation of these peaks and their associated symmetry in the literature. Johnston and Shriver presented strong evidence for differentiation between S−O and C−F bonds.[46] There is minimal variation in the vibrational response under negative potentials (see Figure 4(c)). However, data collected below 0 V is not reported due to significant disturbances at the electrode surface, resulting in unreadable spectra at these potentials.

The positive potential measurements (Figure 4b) reveal minimal change in the symmetric stretching $SO_3$ peak ($\nu_s$ $SO_3$ at 1030 $cm^{-1}$) but increased intensity and complete convergence of $\nu_s$ and $\nu_{as}$ $CF_3$ peaks at 1225 and 1255 $cm^{-1}$. Significant intensity increase follows potentials beyond 1.4 V, with the surge in $CF_3$ vibrations suggesting reorientation of the anion to favor $CF_3$ at the interface, leaving $SO_3$ available for coordination.[51] Such configuration is demonstrated in the molecular dynamics simulation, where the oxygen in $SO_3$ is to coordinate cations, $Zn^{2+}$ in this case, and $CF_3$ is reoriented toward the electrode surface.[51] While increased symmetric stretching suggests tridentate adsorption at the gold electrode surface, increases in asymmetric stretching (see Figure 4(d)) suggests increased interaction with the surrounding electrolyte system as a concentration gradient forms next to the electrode surface.[39,52] The emerging peak at 975 $cm^{-1}$ is associated with OH stretching due to coordination between solvent/cations and the increasing hydrogen bonding network at the electrode surface.[53,54]

Figure 5 displays the potential dependent ATR-SEIRAS spectra for ZnOTF dissolved in a 1:1 $H_2O$:ACN solution. The spectra are relatively unaffected by negative potentials down to 0 V, like the aqueous solution. However, unlike aqueous ZnOTF, the spectra with acetonitrile additive exhibited much less disturbance at zinc reduction potentials. Additional spectra taken at −0.1 V and −0.2 V are shown in Figure 5a, where all OTF peaks are enhanced at these more negative potentials, coinciding with the onset of zinc reduction. The significant enhancement of the IR spectrum is possibly due to the formation of metallic Zn nanostructures and/or increase in the surface area of the electrode open to the electrolyte. Acetonitrile additive in aqueous zinc electrolyte systems has been shown to adsorb to active sites for hydrogen reduction, breaking the hydrogen bond network of the water solvation shell.[21] Meng et al. report that acetonitrile can reduce dendrite growth and offer uniform charge distribution through steady diffusion of $Zn^{2+}$ in a single direction, shielding from tip charge.[21] This decrease in surface disturbance is in keeping with the observations in the SEIRA measurements.


https://doi.org/10.1021/acsami.4c15318
ACS Appl. Mater. Interfaces XXXX, XXX, XXX−XXX

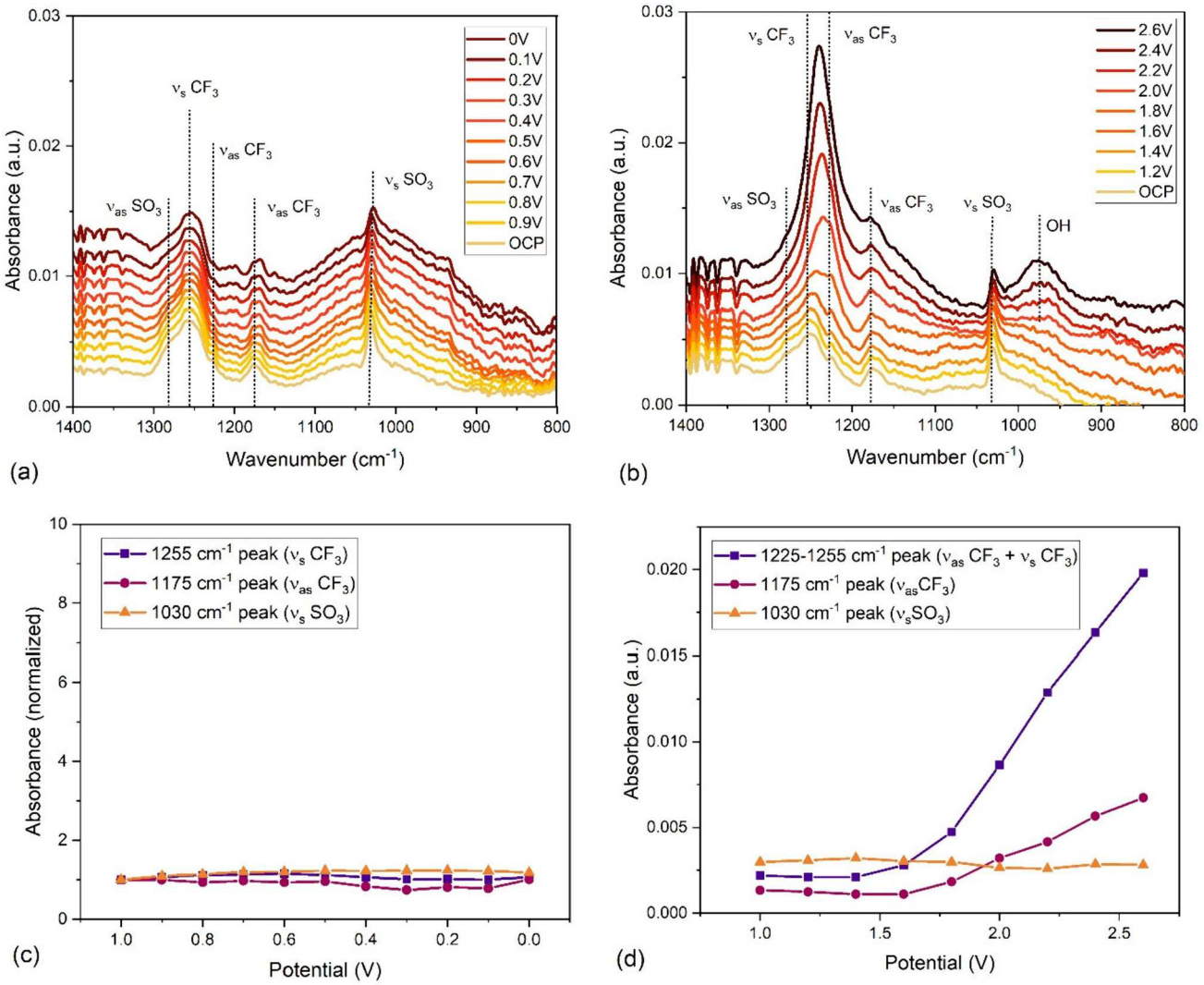


**Figure 4.** Potential dependent ATR-SEIRAS spectra for (a) 1m aqueous ZnOTF at negative potentials and (b) positive potentials. Normalized (intensity of each peak at OCP as reference point) potential dependent scaling of prominent spectral peaks at (c) negative potentials and (d) positive potentials.

To complement the discussion of adsorption, Figures 5c and 5d illustrate changes in the mid-IR frequency stretching peaks associated with the acetonitrile additive.[43] Previous studies have reported that ACN has a higher adhesion energy than water, which facilitates its accumulation at the electrode surface.[8,21] Indeed, the C ≡ N stretching peak at 2255 $cm^{-1}$ is clearly identifiable at OCP (~1 V), accompanied by a weaker combination peak at 2292 $cm^{-1}$ associated with $CH_3$ deformation and C−C stretching. On the contrary to the literature for pure ACN solvents, the intensity of the C ≡ N peak decreases with the application of negative potential, indicating the replacement of ACN with water, salt or both. Reinsberg and Baltruschat previously demonstrated a preference for the orientation of ACN with $CH_3$ perpendicular to the electrode surface, using the application of negative potentials and pure ACN solvent.[24] The decreasing intensity of the C ≡ N peak and the distortion of the $CH_3$ region at higher frequencies suggest the presence of water creates a more complex surface environment. In the bulk solution of 1:1 ACN:$H_2O$ zinc electrolyte, the zinc solvation shell is still primarily water, due to water's higher polarity compared to acetonitrile.[55] The presence of ACN disrupts $Zn^{2+}$-$H_2O$ interactions and the $H_2O$−$H_2O$ hydrogen bonding network, but water molecules still dominate the solvation environment.[21] When negative potential is applied, cations are expected to move toward the surface, into the Helmholtz layer, carrying the water solvation shell with them. We could speculate that this would result in increased water at the surface and decreased overall presence of acetonitrile, as observed in the potential dependent C ≡ N spectral peak.

Despite its decreased presence, ACN significantly impacts the desolvation process at the interface, which is reflected in the increased surface stability at the onset of zinc reduction. The frequency of the C ≡ N peak positioning and lack of Stark shift in the C ≡ N peak is indicative of uncoordinated ACN molecules before the onset of zinc reduction at −0.1 V.[23,24] Previous studies have shown cation-solvent interactions to cause IR peak blue-shift, while anion-solvent interactions cause red-shift.[24,56] The lack of potential dependent shift and the typical frequency of the C ≡ N peak is therefore indicative of little to no coordination with the electrolyte ions at the surface from 1 to 0 V. However, the Stark shift observed at −0.1 V and −0.2 V for C ≡ N stretching peak at 2255 $cm^{-1}$ (Panel c) as well as $\nu_s$ and $\nu_{as}$ $CF_3$ vibrations (Panel a) indicates strong


https://doi.org/10.1021/acsami.4c15318
ACS Appl. Mater. Interfaces XXXX, XXX, XXX−XXX

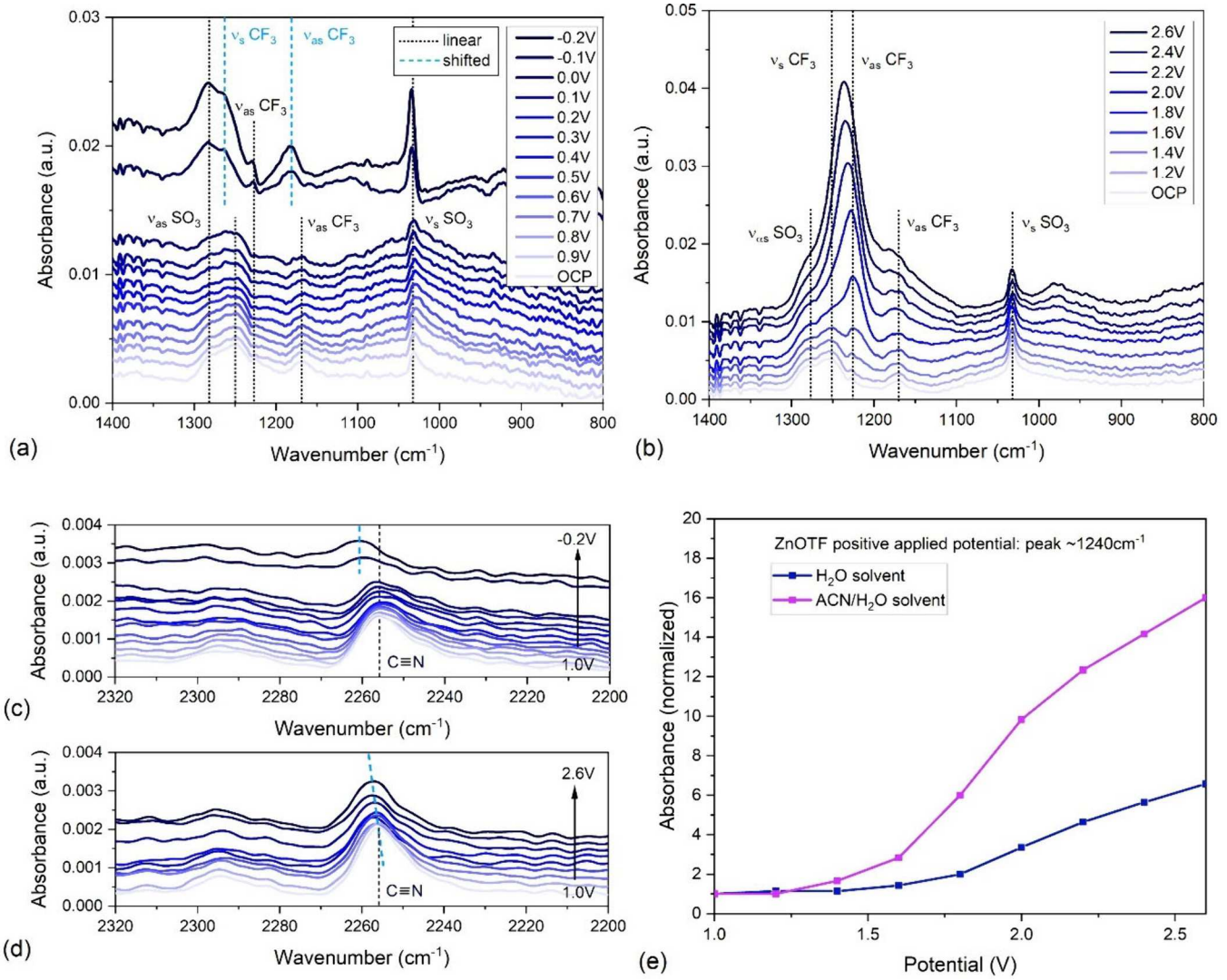


**Figure 5.** ATR-SEIRAS potential dependent spectra for (a) 1m ZnOTF with 1:1 $H_2O$:ACN solvent at negative potentials, (b) positive potentials, (c) mid frequency negative potential acetonitrile peak, (d) mid frequency positive potential acetonitrile peak, and (e) comparison between solvents for positive potential peak ~1225 $cm^{-1}$.

coordination between electrode and ACN/anions at the interface following the onset of zinc reduction.

The SEIRAS measurements for positive potentials applied to ZnOTF with ACN:$H_2O$ solvent (Figure 5b) exhibit results like those of the aqueous electrolyte. The $\nu_{as}$ and $\nu_s$ $CF_3$ peaks rapidly increase in intensity with applied potential and become resolved into a single peak at 1225 $cm^{-1}$. This suggests tridentate adsorption of the $OTF^-$ via $CF_3$ orientation at the interface because of the significant increase in symmetric stretching. The potential dependent intensity of this peak for both the water and ACN:$H_2O$ solvents is compared in Figure 5e. This comparison reveals that the effect of positive potential on the intensity of the $CF_3$ peak is significantly enhanced by the acetonitrile additive. The water solvent sees the $\nu_{as}$ and $\nu_s$ $CF_3$ peaks intensify relatively equally, however the $\nu_{as}$ $CF_3$ asymmetric peak at 1225 $cm^{-1}$ dominates with the ACN additive, suggesting more interaction with neighboring anions due to increased concentration at the surface. Above OCP, water molecules at the surface reorientate to favor their negative dipole toward the electrode surface,[57] promoting the formation of hydrogen bond networks. Since acetonitrile is known to disrupt these networks, it follows that the $OTF^-$ ions are more easily able to approach and adsorb to the surface, showing increased intensity in the associated IR peaks.

A small decrease in the intensity of the C ≡ N peak is observed for positive potentials similar to negative potentials (Figure 5d), suggesting a reduced presence of ACN at the surface, possibly replaced by water and anions. Again, this conflicts with the literature regarding pure ACN solvent, although there is less reported data for acetonitrile as an additive. Sayama et al. report an increased presence of ACN at the electrode under positive potentials, and propose ACN is attracted by an interaction with $OTF^-$ anions adsorbed at the surface.[58] It is likely that the water in the 1:1 $H_2O$:ACN mixed solvent is more favorable for water and solvated ions due to the presence of highly electronegative oxygen at positive potentials.

Acetonitrile water-in-salt (AWIS) electrolytes offer stabilization to zinc electrolyte systems. The SEIRA spectra in the 800−1400 $cm^{-1}$ region, which tracks the potential dependence of S═O, S−N−S, and C−F bonds, is reported in Figure 6.[59,60] When the negative potential is applied (Panel (a) and (c), Figure 6), there is a small overall change in the system, with less preference toward the $CF_3$ end of the $TFSI^-$ ions at the surface. From 1 V down to 0.2 V there is a small increase in


https://doi.org/10.1021/acsami.4c15318
ACS Appl. Mater. Interfaces XXXX, XXX, XXX−XXX

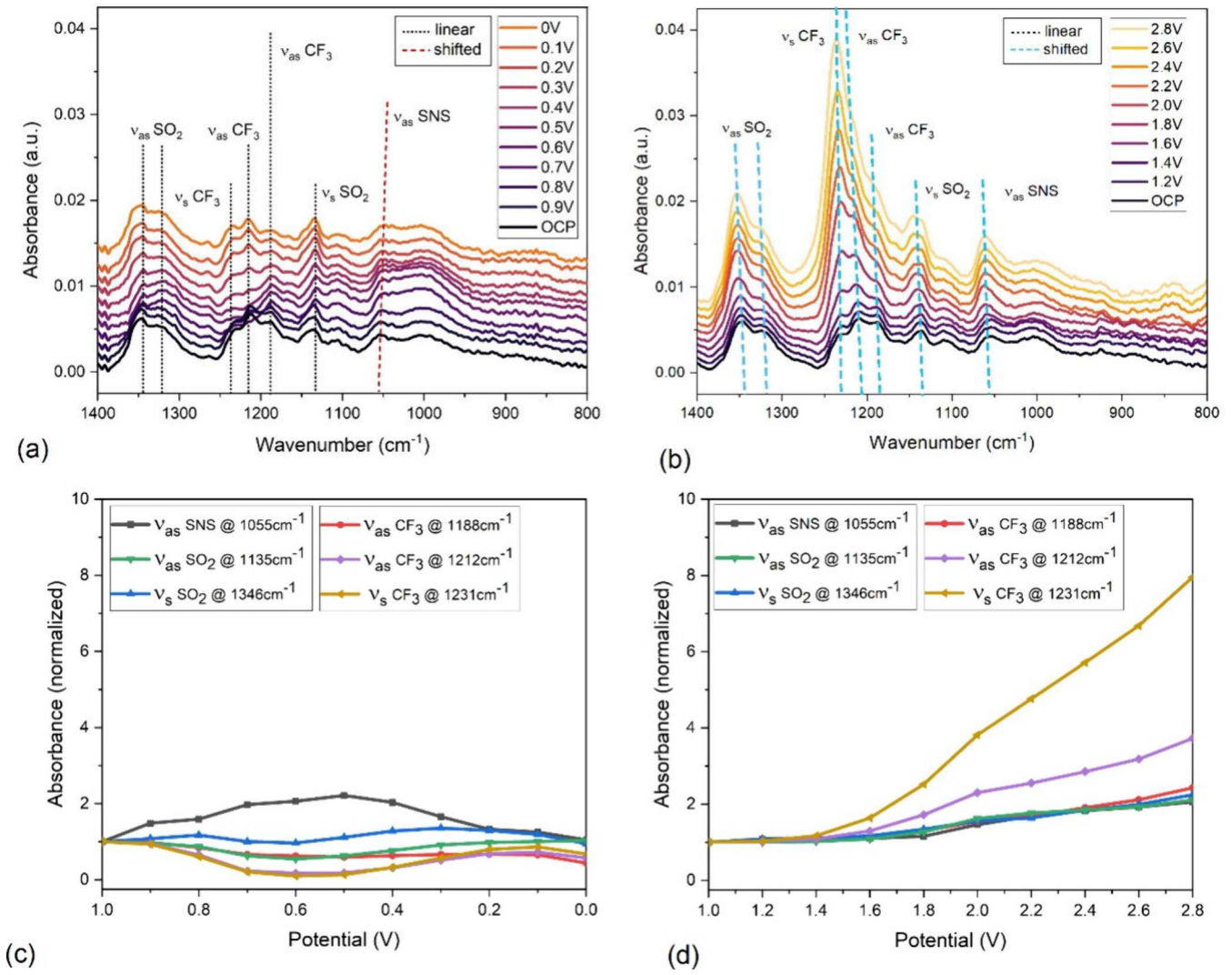


**Figure 6.** ATR-SEIRAS potential dependent spectra for 5m Zn AWIS electrolyte at (a) negative potentials and (b) positive potentials. Normalized (intensity of each peak at OCP as reference point) potential dependent scaling of prominent spectral peaks at (c) negative potentials and (d) positive potentials.

peak intensity for the S−N−S vibrational mode, alongside a drop in the $CF_3$ stretching, indicating a rotation of the anion in response to the negative surface. Beyond 0.2 V the anion moves away from the surface, with all peaks dropping in intensity. These changes are suggestive of the bulk solution only and not surface adsorption, due to the small effect of potential on peak absorbance. Beyond 0 V, the interface exhibits exceptional stability with large intensity spikes into zinc reduction (see Figure S1) The lack of disturbance in the spectra indicates the continued integrity of the anion adsorption, undisturbed by the hydrogen evolution experienced by other electrolytes.

In the positive direction, all $TFSI^-$ peak intensities increased with potential, demonstrating the increased presence of the anion at the electrode surface (Figure 6 (b) and (d)). While the $SO_2$ and $CF_3$ peaks begin at similar intensities at OCP, the $CF_3$ peaks increased most at positive potentials, with the $\nu_{as}$ $CF_3$ peak at 1231 $cm^{-1}$ experiencing the largest increase. The surge in $CF_3$ vibrations beyond 1.4 V suggests the anion favors $CF_3$ at the interface over $SO_2$ at these potentials. $TFSI^-$ has been shown to adsorb with the longest axis parallel to the surface, via one $SO_2$ group, while the other $SO_2$ remains away from the surface and available for coordination with cations, however the possibility for orientation via the $CF_3$ at high potential could be considered.[51,61] Hoane et al. report increased presence of $TFSI^-$ at positive potentials for an aqueous 1m water-in-salt electrolyte but with uniform growth from all vibrational modes.[60] Although the acetonitrile and differing concentration do not allow a direct comparison, it is noteworthy that this study performed SEIRAS up to 1.4 V and not beyond where we observe a surge in $CF_3$ vibrations. Consistently clear spectra were measured up to 2.8 V, beyond potentials measured for the other electrolytes, showing an increased potential window and continued stability at the surface.

**EQCM-D Measurements.** EQCM-D measurements for 1 m aqueous $ZnSO_4$ are presented in Figure 7a. During the 5 cycles of CV, more mass is accumulated at the electrode with each cycle (top and bottom, Figure 7a). This happens in two potential dependent steps. The initial mass increase is observed at ∼0.4 V, coinciding with the sharp rise in $SO_4$ peak intensities seen in the IR spectrum (Panel (a), Figure 3). As previously reported, the adsorbed layer likely consists of solvated cations in the form of adsorbed $Zn_4SO_4(OH)_6$·


https://doi.org/10.1021/acsami.4c15318
ACS Appl. Mater. Interfaces XXXX, XXX, XXX−XXX

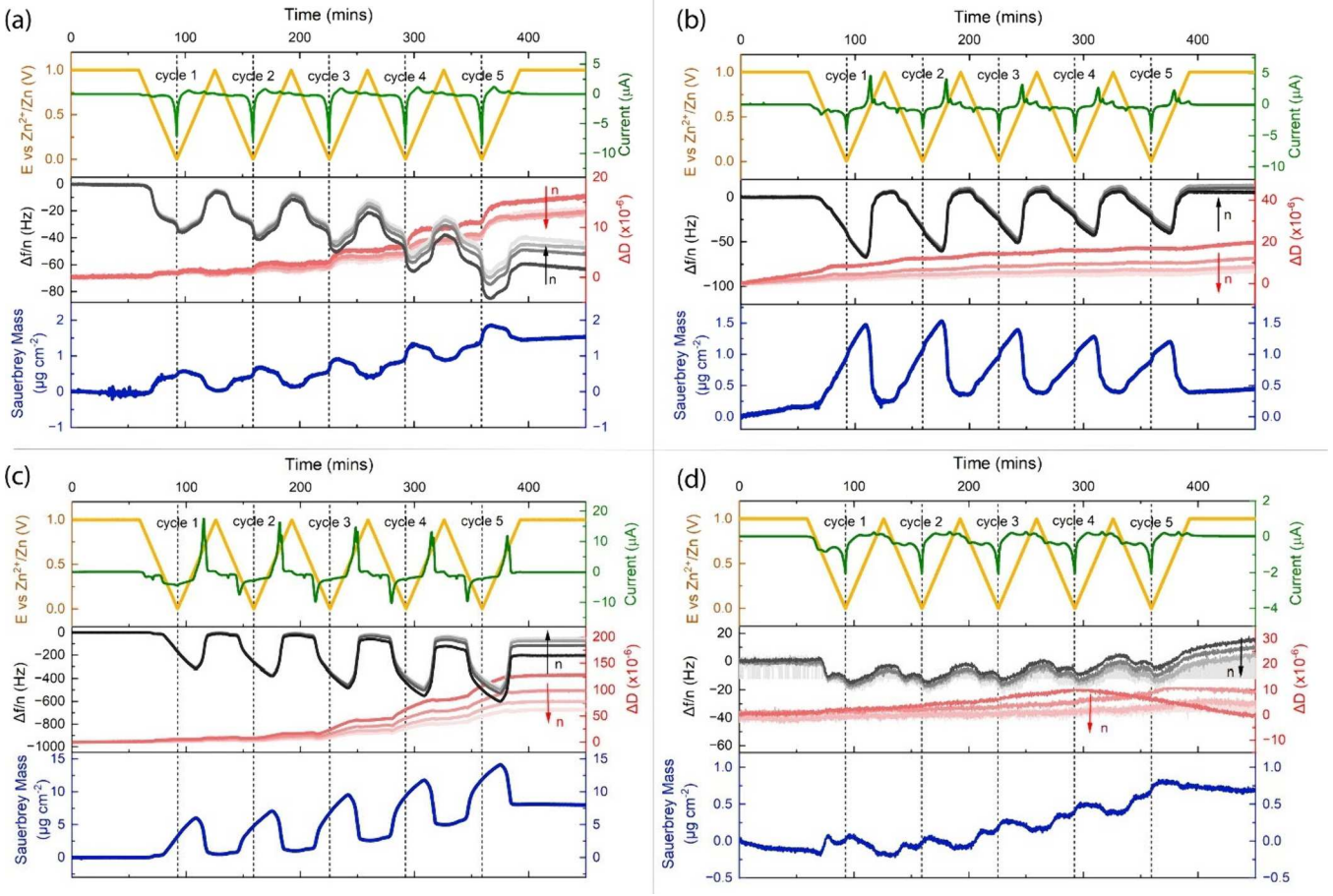


**Figure 7.** EQCM-D measurements for (a) 1m aqueous $ZnSO_4$ electrolyte, (b) 1m aqueous ZnOTF, (c) 1m ZnOTF with 1:1 $H_2O$:ACN solvent, (d) 5m Zn AWIS electrolyte. Time dependent cyclic voltammograms are shown at the top of each panel, in-line with frequency change (black curves, left axis) and dissipation change (red curves, right axis) for overtones 3, 5, 7, 9. Mass determined by Sauerbrey equation is shown in blue (bottom of each panel).

$xH_2O$.[62] At ~ 0 V a second increase in mass is observed at the onset of zinc reduction, where zinc can adsorb directly to the electrode surface. As the cycle progresses, mass desorbs from the surface, but does not fully return to its preadsorption value, indicating the formation of a Zn interphase layer. The generation of $Zn_4SO_4(OH)_6{\cdot}xH_2O$ in mildly acidic $ZnSO_4$ electrolyte is reported in the literature, however, due to its loose and porous nature, it does not act as a useful passivation layer and ultimately results in continued corrosion of deposited zinc and battery failure.[43]

Dissipation measurements enable the determination of the film's rigidity. The aqueous $ZnSO_4$ initially shows low magnitudes of $\Delta D$ (e.g., $< 3 \times 10^{-6}$), indicating the small volume of the deposited film remains rigid until the third cycle when it starts to show signs of viscoelasticity or porosity (see red lines, center panel, Figure 7a).[29] The stepped increase in dissipation becomes more prominent with additional cycles, while the reduction current increases, indicating the evolution of a porous interphase layer. Schick et al. report similar observations for the deposition of a porous Mg interphase.[63] The spreading of $\Delta D$ overtones can be attributed to zinc deposition permeating the interphase pores, which slows the dissolution process and increases the depth of the porous layer.[64]

While $\Delta D$ values do increase with cycling, the values are still low in magnitude for the full 5 cycles measured (e.g., $< 20 \times 10^{-6}$), and the $\Delta D_n/(\Delta f_n/n)$ ratio is small enough (e.g., < 0.3 $\mu$Hz) that the Saurbrey equation can still be considered valid for quantifying mass of the deposited film.[29] The deposited mass calculated using the Sauerbrey equation and the fundamental frequency was 1.47 $\mu g\ cm^{-2}$ after five cycles (blue line, bottom, Figure 7a). It is noteworthy that there is no change in the spread between dissipation overtones observed at 0.4 V, where frequency and mass measurements increase and decrease through the cycles. An increased spread between dissipation overtones is only significant after 0 V with each cycle, where zinc stripping occurs. This observation correlates with the porous nature of adsorbed $Zn_4SO_4(OH)_6{\cdot}xH_2O$ as the depth of the adsorbed layer increases. The spreading of both $\Delta D$ and $\Delta f/n$ after cycle 3 demonstrates that as layers are deposited with increased depth, they vary in structure, and the rigid layer deposited with early cycles becomes softer/porous over time.[65]

The porosity of the upper layer permits continued zinc deposition and dissolution without decreasing the associated reduction current over the five cycles measured. Instead, a small increase in current is observed in both the EQCM-D cyclic voltammogram and that taken using the spectroelectrochemical cell. This observation is corroborated by the magnitude of the zinc reduction mass step at 0 V through the five reported cycles. While the largest adsorption of $Zn_4SO_4(OH)_6{\cdot}xH_2O$ can be seen in the first cycle, the largest


https://doi.org/10.1021/acsami.4c15318
ACS Appl. Mater. Interfaces XXXX, XXX, XXX−XXX

zinc deposition step can be seen in the fifth cycle. Although these observations are suggestive of an SEI layer that is useful for the overall efficiency of the electrolyte, limited Coulombic efficiency and growth of "dead" zinc at the electrode surface are commonly reported for the long-term cycling of zinc sulfate.

EQCM-I measurements for 1m aqueous ZnOTF are presented in Figure 7b. Mass begins to adsorb at 0.75 V and desorbs at 0.5 V, with adsorption more continuous and steady compared to $ZnSO_4$. The ZnOTF electrolyte exhibits a minor drift in frequency over time in repeated EQCM-D experiments, regardless of the applied potential. This phenomenon was not observed for the other electrolytes. The calculated Sauerbrey mass following 5 cycles aligns with this continuous drift, indicating no significant permanently adsorbed layer due to applied potential. It should be noted, however, that the $\Delta D_n/(\Delta f_n/n)$ ratio (e.g., > 1 $\mu$Hz after 5 cycles), indicates some viscoelasticity at the surface. There is minimal spreading between overtones for $\Delta f_n/n$ showing uniformity in the interface without structural difference through the surface at the electrode. The continuous spread between $\Delta D$ overtones suggests increased viscosity of the electrolyte solution within the short-range of the quartz crystal sensor rather than that of a deposited film due to applied potential. The only noteworthy step in $\Delta D$ is seen in the first cycle at 0.6 V, suggesting there is a small structural change in the electrolyte/electrode interface.

No surface changes were observed at 0.6 V in the IR spectra (Figure 4(c)) leading up to deposition. However, the decreasing stripping current with each cycle seen in the EQCM CV (top panel, Figure 7a) suggests inefficiency in the removal of deposited reduction products. A slowing of charge transfer, the "liquid-like" response of the EQCM-D, coupled with the lack of spectral changes, suggests increased viscosity of the diffuse double layer rather than a solid adsorbed layer.[66]

For comparison with the aqueous electrolyte, EQCM-D measurements for 1m ZnOTF in 1:1 $H_2O$:ACN solvent are shown in Figure 7c. The interface condition is more stable than the aqueous ZnOTF electrolyte with no drift/change in $\Delta D$ or $\Delta f_n/n$ until the negative potential is applied. Following the first cycle, a negative current is observed at 0.4 V, coinciding with a step in mass that partially remains following dissolution. This potential is substantially above zinc reduction, and due to the enlarged potential window observed with the ACN additive (Figure 2), minimal current (and no deposition) is observed at 0 V. The permanent surface changes seen at 0.4 V for adsorption/desorption can therefore be associated with the formation of a passivation interphase layer.

Both mass and dissipation measurements are of higher magnitude than the two purely aqueous electrolytes (×5), showing a notable deposition of a viscoelastic or porous interphase layer. The $\Delta D_n/(\Delta f_n/n)$ ratio increases from the first dissolution step at 0.4 V (120 min, Figure 7c), and the viscoelastic properties of the deposited layer continue to climb with each cycle. The n = 3 overtone, which describes the outer region of the deposited layer, showed $\Delta D_3/(\Delta f_3/3)$ reaching 0.6 $\mu$Hz while additional overtones, responding to regions closest to the interface reach magnitudes of 1 $\mu$Hz.

The spreading of both $\Delta D$ and $\Delta f_n/n$ overtones describes a multilayered composition with outer layers becoming more porous or viscoelastic with each cycle. Substantial mass is deposited at the surface with each cycle, however, due to the porous/viscoelastic nature of the structure, the Sauerbrey equation can not be reliably used for quantification. Future study with a hydrodynamic (used for porous layers) and viscoelastic modeling (used for viscoelastic layers) is required to make an informed conclusion about the composition this passivation layer and it is impact of long-term stability for battery applications. A deeper understanding of any viscoelastic properties is of particular interest, because such layers have the advantage of reduced cracking and surface defects.[67]

The tendency for ACN to adsorb at the interface, coupled with the increased mass and reduced intensity of the C ≡ N spectral peak, raises questions about the structure of this observed passivation layer. It has been previously reported that organic additives can reduce the desolvation energy of $Zn^{2+}$ and that coordination between adsorbed ACN and cations impacts spectral peak intensity and position.[24,62] The formation of chained networked structures has been reported in acetonitrile solvent for lithium battery passivation layers, where a complex of all solvent molecules forms with increased viscosity.[68] It is possible that Zinc battery electrolytes form a similar complex, acting as SEI for improved battery performance. More investigation into the ACN-ZnOTF passivation layer is required to confirm this hypothesis.

EQCM-I measurements for 5m Zn AWIS are depicted in Figure 7d. Mass accumulation is observed at 0.6 V in the first cycle and again approaching zinc reduction (0 V). Although mass deposited in the first cycle appears fully dissolved at a positive potential, for subsequent cycles, the mass adsorbed remains at the surface, increasing with every cycle. It has previously been reported that highly concentrated zinc water-in-salt electrolytes can produce thin compact functional SEI layers, and do not produce porous passivation layers like those found in aqueous and dilute electrolytes.[69] There is a small increase in dissipation for the first 3 cycles (e.g., $\Delta D < 10 \times 10^{-6}$), and measurements taken at the outer surface of the deposited layer (overtone n = 3) show decreased dissipation from cycle 4, reaching zero after cycle 5 (red curves, middle, Figure 7d). This is indicative of a double layered interphase, with a rigid outer surface that can be characterized as a physical SEI.

SEIRAS measurements (Figure 6) show the reorganization of $TFSI^-$ ions in the same region as the accumulation of mass and increased current (0.6 V) but can not confirm the formation of new species. Reported in situ formation of SEI in lithium-ion batteries relies on the decomposition of anions and organic solvents to form highly permeable complexes at the electrode/electrolyte interface.[70] The higher redox potential of zinc makes this unlikely in zinc-ion batteries, and therefore an investigation into in situ zinc SEIs is still ongoing. Qiu et al. reported the formation of a $ZnF_2$ SEI layer along with problematic ZnO deposition for a similar $Zn(TFSI)_2$/ACN eutectic solution using Raman and XPS.[70] The associated spectral peaks are outside of the detection range for SEIRAS and therefore the presence of an $ZnF_2$ based SEI for this study cannot be confirmed.

$\Delta f_n/n$ measurements and the spread between overtones are of low magnitude and can be seen to drift into positive $\Delta f_n/n$ values for overtones beyond the fundamental (n = 3−9 shown, middle Figure 7d). These overtones are used to understand the structural properties through the depth of the deposited film,[30,31] while the fundamental frequency was used to calculate the mass (blue curve, bottom, Figure 7d). While a thin rigid film of low mass can be reported (0.7 $\mu$g cm$^{-2}$ after 5 cycles), the relationship response for higher overtones does not offer a clear understanding of the interphase beyond.


https://doi.org/10.1021/acsami.4c15318
ACS Appl. Mater. Interfaces XXXX, XXX, XXX−XXX

## 5. CONCLUSION

Three zinc electrolyte salts were compared using potential dependent ATR-SEIRAS and EQCM-I measurements to elucidate the mechanisms of surface interactions and passivation layer formation. The findings are critical for the development of ZIBs, which are gaining attention due to zinc's high capacity density, nontoxicity, and improved eco-efficiency compared to other battery systems. SEIRAS measurements for $ZnSO_4$ exhibited an increased presence of $SO_4^{2-}$ ions at the interface following applied negative potentials, while the EQCM-D measurements measured a porous passivation layer accumulating after the onset of zinc deposition and dissolution. This structure is attributed to the formation of a $Zn_4SO_4(OH)_6{\cdot}xH_2O$ complex, which, despite its corrosive nature in long-term cycling, enhanced current efficiency over the five measured cycles. Despite the porous properties of the deposited layer, the $\Delta D_n/(\Delta f_n/n)$ ratio showed the Sauerbrey equation to be valid for mass calculation, which is reported as 1.47 $\mu$g cm$^{-2}$ after five cycles. SEIRAS measurements with positive applied potential showed an increased presence of $HSO_4^-$ vibrations associated with adsorbed protonated sulfate ions in the form of bisulfate and/or hydrate complexes. Measurements show a significant blue shift in nearby weak/broad $SO_4^{2-}$ peaks not adsorbed at the surface due to vibrational Stark shift.

ZnOTF, tested in both aqueous form and with a 1:1 $H_2O$:ACN solvent, demonstrated rapid intensity increases in $CF_3$ spectral peaks at positive potentials, suggesting adsorption of the $OTF^-$ anion at the electrode surface, arranged with fluoride atoms orientated toward the surface. The presence of acetonitrile additive enhanced adsorption, demonstrating its ability to disrupt water's hydrogen bonding networks and facilitate surface changes. At negative potentials, the acetonitrile additive improved electrode stability, preventing hydrogen evolution and forming a porous or viscoelastic passivation layer. EQCM-D measurements showed both mass and dissipation of higher magnitude (×5) than both the aqueous electrolytes, with a spread of $\Delta D$ and $\Delta f_n/n$ overtones. A multilayered passivation layer is observed with the upper, newly deposited region more rigid than layers that have experienced multiple cycles. Due to the porous or viscoelastic nature of the structure, the Sauerbrey equation can not be reliably used for the quantification of mass. While no new species were detected through decomposition, it is hypothesized that a coordination network forms near the surface, similar to structures reported in lithium-ion batteries, warranting further investigation to confirm the composition of the deposited mass.

The Zn AWIS hybrid electrolyte exhibited increased intensity for all peaks at a positive potential, with $CF_3$ vibrations experiencing a significant surge beyond 1.4 V. Increased spectral peaks and a notable potential dependent blue shift is associated with adsorbance at the electrode, however it is still unclear whether the anion orientates with a $CF_3$ or $SO_2$ group at the interface. The gold electrode showed exceptional stability at negative potentials into zinc reduction, enhancing ZIB performance by preventing hydrogen evolution. EQCM-D measurements demonstrated mass accumulation with low magnitude $\Delta D/(\Delta f_n/n)$ ratios through all overtones. A compact rigid SEI layer of 0.7 $\mu$g cm$^{-2}$ was calculated using the Sauerbrey equation, with dissipation at the outer region of the layer (n = 3) dropping to zero in the fourth cycle. The deposited layer is observed to form at 0.6 V in the first cycle and is tentatively attributed to the formation of a $ZnF_2$ SEI layer, though confirmation was outside the wavenumber range of SEIRAS.

This study has demonstrated the formation of porous passivation layers for all tested electrolytes, with acetonitrile shown to reduce electrode disturbances and facilitate surface adsorption of anions. The development of acetonitrile−water-in-salt electrolytes shows promise in the in situ formation of SEIs to address the ongoing issue of hydrogen evolution and dendrite formation in ZIBs. Future work will focus on the structure of these deposited layers and methods to identify properties of in situ SEIs to enhance ZIB performance, providing a path toward more stable and efficient energy storage solutions. These findings contribute to the broader goal of developing viable long-term solutions for clean, high-capacity energy storage, supporting the transition to renewable energy sources.

## ■ ASSOCIATED CONTENT

### Supporting Information

The Supporting Information is available free of charge at https://pubs.acs.org/doi/10.1021/acsami.4c15318.

Additional potential dependent ATR-SEIRAS spectra data for the 5m Zn AWIS electrolyte (PDF)

## ■ AUTHOR INFORMATION


### Corresponding Author

**Zhange Feng** − *Department of Chemistry and Biochemistry, University of Nevada, Las Vegas, Nevada 89154, United States;* orcid.org/0009-0006-5664-531X; Email: zhange.feng@unlv.edu

### Authors

**Katherine Betts** − *Department of Chemistry and Biochemistry, University of Nevada, Las Vegas, Nevada 89154, United States;* orcid.org/0009-0004-7412-1806

**Yuhan Jiang** − *Department of Chemistry and Biochemistry, University of Nevada, Las Vegas, Nevada 89154, United States*

**Michael Frailey** − *Department of Chemistry and Biochemistry, University of Nevada, Las Vegas, Nevada 89154, United States*

**Kidus Yohannes** − *Department of Chemistry and Biochemistry, University of Nevada, Las Vegas, Nevada 89154, United States*

Complete contact information is available at: https://pubs.acs.org/10.1021/acsami.4c15318


### Notes

The authors declare no competing financial interest.

## ■ ACKNOWLEDGMENTS

This work is supported by a grant from NSF (CBET-2243098).

## ■ REFERENCES

(1) Larcher, D.; Tarascon, J.-M. Towards Greener and More Sustainable Batteries for Electrical Energy Storage. *Nat. Chem.* **2015**, 7 (1), 19−29.

(2) Liang, Y.; Dong, H.; Aurbach, D.; Yao, Y. Current Status and Future Directions of Multivalent Metal-Ion Batteries. *Nat. Energy* **2020**, *5* (9), 646−656.
(3) Song, M.; Tan, H.; Chao, D.; Fan, H. J. Recent Advances in Zn-Ion Batteries. *Adv. Funct. Mater.* **2018**, *28* (41), 1802564.
(4) Huang, J.; Qiu, X.; Wang, N.; Wang, Y. Aqueous Rechargeable Zinc Batteries: Challenges and Opportunities. *Curr. Opin. Electrochem.* **2021**, *30*, 100801.
(5) Sun, Z.; Bu, F.; Zhang, Y.; Zhou, W.; Li, X.; Liu, X.; Jin, H.; Ding, S.; Zhang, T.; Wang, L.; Li, H.; Li, W.; Zhang, C.; Zhao, D.; Wang, Y.; Chao, D. Electron-Donating Conjugation Effect Modulated Zn2+ Reduction Reaction for Separator-Free Aqueous Zinc Batteries. *Angew. Chem., Int. Ed.* **2024**, *63* (20), No. e202402987.
(6) Bu, F.; Sun, Z.; Zhou, W.; Zhang, Y.; Chen, Y.; Ma, B.; Liu, X.; Liang, P.; Zhong, C.; Zhao, R.; Li, H.; Wang, L.; Zhang, T.; Wang, B.; Zhao, Z.; Zhang, J.; Li, W.; Ibrahim, Y. S.; Hassan, Y.; Elzatahry, A.; Chao, D.; Zhao, D. Reviving Zn0 Dendrites to Electroactive Zn2+ by Mesoporous MXene with Active Edge Sites. *J. Am. Chem. Soc.* **2023**, *145* (44), 24284−24293.
(7) Wang, X.; Sun, C.; Wu, Z.-S. Recent Progress of Dendrite-Free Stable Zinc Anodes for Advanced Zinc-Based Rechargeable Batteries: Fundamentals, Challenges, and Perspectives. *SusMat* **2023**, *3* (2), 180−206.
(8) Shi, J.; Xia, K.; Liu, L.; Liu, C.; Zhang, Q.; Li, L.; Zhou, X.; Liang, J.; Tao, Z. Ultrahigh Coulombic Efficiency and Long-Life Aqueous Zn Anodes Enabled by Electrolyte Additive of Acetonitrile. *Electrochim. Acta* **2020**, *358*, 136937.
(9) Osawa, M. Dynamic Processes in Electrochemical Reactions Studied by Surface-Enhanced Infrared Absorption Spectroscopy (SEIRAS). *Bull. Chem. Soc. Jpn.* **1997**, *70* (12), 2861−2880.
(10) Osawa, M.; Ataka, K. Electromagnetic Mechanism of Enhanced Infrared Absorption of Molecules Adsorbed on Metal Island Films. *Surf. Sci.* **1992**, *262* (3), L118−L122.
(11) Ataka, K.; Stripp, S. T.; Heberle, J. Surface-Enhanced Infrared Absorption Spectroscopy (SEIRAS) to Probe Monolayers of Membrane Proteins. *Biochim. Biophys. Acta BBA - Biomembr.* **2013**, *1828* (10), 2283−2293.
(12) Chang, X.; Vijay, S.; Zhao, Y.; Oliveira, N. J.; Chan, K.; Xu, B. Understanding the Complementarities of Surface-Enhanced Infrared and Raman Spectroscopies in CO Adsorption and Electrochemical Reduction. *Nat. Commun.* **2022**, *13* (1), 2656.
(13) Morhart, T. A.; Unni, B.; Lardner, M. J.; Burgess, I. J. Electrochemical ATR-SEIRAS Using Low-Cost, Micromachined Si Wafers. *Anal. Chem.* **2017**, *89* (21), 11818−11824.
(14) Zhumaev, U.; Rudnev, A. V.; Li, J.-F.; Kuzume, A.; Vu, T.-H.; Wandlowski, T. Electro-Oxidation of Au(111) in Contact with Aqueous Electrolytes: New Insight from in Situ Vibration Spectroscopy. *Electrochim. Acta* **2013**, *112*, 853−863.
(15) Bhattacharyya, D.; Videla, P. E.; Cattaneo, M.; Batista, V. S.; Lian, T.; Kubiak, C. P. Vibrational Stark Shift Spectroscopy of Catalysts under the Influence of Electric Fields at Electrode-Solution Interfaces. *Chem. Sci.* **2021**, *12* (30), 10131−10149.
(16) Feldt, C. D.; Moreira, R.; Meyer, E.; Clawin, P.; Riedel, W.; Risse, T.; Moskaleva, L.; Dononelli, W.; Klüner, T. CO Adsorption on Au(332): Combined Infrared Spectroscopy and Density Functional Theory Study. *J. Phys. Chem. C* **2019**, *123* (13), 8187−8197.
(17) Pfisterer, J. H. K.; Zhumaev, U. E.; Cheuquepan, W.; Feliu, J. M.; Domke, K. F. Stark Effect or Coverage Dependence? Disentangling the EC-SEIRAS Vibrational Shift of Sulfate on Au(111). *J. Chem. Phys.* **2019**, *150* (4), 041709.
(18) Ma, Y.; Zhang, Q.; Liu, L.; Li, Y.; Li, H.; Yan, Z.; Chen, J. N,N-Dimethylformamide Tailors Solvent Effect to Boost Zn Anode Reversibility in Aqueous Electrolyte. *Natl. Sci. Rev.* **2022**, *9* (10), nwac051.
(19) Ilic, S.; Counihan, M. J.; Lavan, S. N.; Yang, Y.; Jiang, Y.; Dhakal, D.; Mars, J.; Antonio, E. N.; Kitsu Iglesias, L.; Fister, T. T.; Zhang, Y.; Maginn, E. J.; Toney, M. F.; Klie, R. F.; Connell, J. G.; Tepavcevic, S. Effect of Antisolvent Additives in Aqueous Zinc Sulfate Electrolytes for Zinc Metal Anodes: The Case of Acetonitrile. *ACS Energy Lett.* **2024**, *9* (1), 201−208.
(20) Rudnev, A. V.; Molodkina, E. B.; Danilov, A. I.; Polukarov, Yu. M.; Berna, A.; Feliu, J. M. Adsorption Behavior of Acetonitrile on Platinum and Gold Electrodes of Various Structures in Solution of 0.5 M H2SO4. *Electrochim. Acta* **2009**, *54* (14), 3692−3699.
(21) Meng, C.; He, W.; Kong, Z.; Liang, Z.; Zhao, H.; Lei, Y.; Wu, Y.; Hao, X. Multifunctional Water-Organic Hybrid Electrolyte for Rechargeable Zinc Ions Batteries. *Chem. Eng. J.* **2022**, *450*, 138265.
(22) Faguy, P. W.; Fawcett, W. R.; Liu, G.; Motheo, A. J. A Study of the Adsorption of Acetonitrile on a Gold Electrode from Aqueous Solutions Using in Situ Vibrational Spectroscopy. *J. Electroanal. Chem.* **1992**, *339* (1), 339−353.
(23) Takamuku, T.; Tabata, M.; Yamaguchi, A.; Nishimoto, J.; Kumamoto, M.; Wakita, H.; Yamaguchi, T. Liquid Structure of Acetonitrile-Water Mixtures by X-Ray Diffraction and Infrared Spectroscopy. *J. Phys. Chem. B* **1998**, *102* (44), 8880−8888.
(24) Reinsberg, P. H.; Baltruschat, H. Potential- and Cation-Dependent Adsorption of Acetonitrile on Gold Investigated via Surface Enhanced Infrared Absorption Spectroscopy. *Electrochim. Acta* **2020**, *334*, 135609.
(25) Ludwig, T.; Singh, A. R.; Nørskov, J. K. Acetonitrile Transition Metal Interfaces from First Principles. *J. Phys. Chem. Lett.* **2020**, *11* (22), 9802−9811.
(26) Solomun, T.; Christmann, K.; Baumgaertel, H. Interaction of Acetonitrile and Benzonitrile with the Gold (100) Surface. *J. Phys. Chem.* **1989**, *93* (20), 7199−7208.
(27) Sauerbrey, G. Verwendung von Schwingquarzen zur Wägung dünner Schichten und zur Mikrowägung. *Z. Für Phys.* **1959**, *155* (2), 206−222.
(28) Voinova, M. V.; Jonson, M.; Kasemo, B. 'Missing Mass' Effect in Biosensor's QCM Applications. *Biosens. Bioelectron.* **2002**, *17* (10), 835−841.
(29) Reviakine, I.; Johannsmann, D.; Richter, R. P. Hearing What You Cannot See and Visualizing What You Hear: Interpreting Quartz Crystal Microbalance Data from Solvated Interfaces. *Anal. Chem.* **2011**, *83* (23), 8838−8848.
(30) Easley, A. D.; Ma, T.; Eneh, C. I.; Yun, J.; Thakur, R. M.; Lutkenhaus, J. L. A Practical Guide to Quartz Crystal Microbalance with Dissipation Monitoring of Thin Polymer Films. *J. Polym. Sci.* **2022**, *60* (7), 1090−1107.
(31) Alexander, T. E.; Lozeau, L. D.; Camesano, T. A. QCM-D Characterization of Time-Dependence of Bacterial Adhesion. *Cell Surf.* **2019**, *5*, 100024.
(32) Rodahl, M.; Höök, F.; Fredriksson, C.; Keller, C. A.; Krozer, A.; Brzezinski, P.; Voinova, M.; Kasemo, B. Simultaneous Frequency and Dissipation Factor QCM Measurements of Biomolecular Adsorption and Cell Adhesion. *Faraday Discuss.* **1997**, *107* (0), 229−246.
(33) Shpigel, N.; Levi, M. D.; Sigalov, S.; Daikhin, L.; Aurbach, D. In Situ Real-Time Mechanical and Morphological Characterization of Electrodes for Electrochemical Energy Storage and Conversion by Electrochemical Quartz Crystal Microbalance with Dissipation Monitoring. *Acc. Chem. Res.* **2018**, *51* (1), 69−79.
(34) Lee, S.; Kang, I.; Kim, J.; Kim, S. H.; Kang, K.; Hong, J. Real-Time Visualization of Zn Metal Plating/Stripping in Aqueous Batteries with High Areal Capacities. *J. Power Sources* **2020**, *472*, 228334.
(35) Coustan, L.; Shul, G.; Bélanger, D. Electrochemical Behavior of Platinum, Gold and Glassy Carbon Electrodes in Water-in-Salt Electrolyte. *Electrochem. Commun.* **2017**, *77*, 89−92.
(36) Peak, D.; Ford, R. G.; Sparks, D. L. An in Situ ATR-FTIR Investigation of Sulfate Bonding Mechanisms on Goethite. *J. Colloid Interface Sci.* **1999**, *218* (1), 289−299.
(37) Franguelli, F. P.; Barta-Holló, B.; Petruševski, V. M.; Sajó, I. E.; Klébert, S.; Farkas, A.; Bódis, E.; Szilágyi, I. M.; Pawar, R. P.; Kótai, L. Thermal Decomposition and Spectral Characterization of Di-[Carbonatotetraamminecobalt(III)] Sulfate Trihydrate and the Nature of Its Thermal Decomposition Products. *J. Therm. Anal. Calorim.* **2021**, *145* (6), 2907−2923.


https://doi.org/10.1021/acsami.4c15318
ACS Appl. Mater. Interfaces XXXX, XXX, XXX−XXX

(38) Müller, K.; Lefèvre, G. Vibrational Characteristics of Outer-Sphere Surface Complexes: Example of Sulfate Ions Adsorbed onto Metal (Hydr)Oxides. *Langmuir* **2011**, *27* (11), 6830−6835.
(39) Chesalov, Y. A.; Andrushkevich, T. V.; Sobolev, V. I.; Chernobay, G. B. FTIR Study of β-Picoline and Pyridine-3-Carbaldehyde Transformation on V-Ti-O Catalysts. The Effect of Sulfate Content on β-Picoline Oxidation into Nicotinic Acid. *J. Mol. Catal. Chem.* **2013**, *380*, 118−130.
(40) Venkatachalam, S.; Jacob, T. DFT Studies on the Nature of Coadsorbates on SO42-/Au(111). *Z. Für Phys. Chem.* **2007**, *221* (9−10), 1393−1406.
(41) Wandlowski, T.; Ataka, K.; Pronkin, S.; Diesing, D. Surface Enhanced Infrared Spectroscopy—Au(1 1 1−20 Nm)/Sulphuric Acid—New Aspects and Challenges. *Electrochim. Acta* **2004**, *49* (8), 1233−1247.
(42) Kwon, K. Y.; Kim, S. J.; Kim, D.-M.; Kim, H.; Mohanty, S. K.; Lee, K. T.; Yoo, H. D. Potential-Dependent Passivation of Zinc Metal in a Sulfate-Based Aqueous Electrolyte. *Langmuir* **2021**, *37* (45), 13218−13224.
(43) Hao, J.; Li, X.; Zhang, S.; Yang, F.; Zeng, X.; Zhang, S.; Bo, G.; Wang, C.; Guo, Z. Designing Dendrite-Free Zinc Anodes for Advanced Aqueous Zinc Batteries. *Adv. Funct. Mater.* **2020**, *30* (30), 2001263.
(44) Yacovitch, T. I.; Wende, T.; Jiang, L.; Heine, N.; Meijer, G.; Neumark, D. M.; Asmis, K. R. Infrared Spectroscopy of Hydrated Bisulfate Anion Clusters: $HSO4^-(H2O)1−16$. *J. Phys. Chem. Lett.* **2011**, *2* (17), 2135−2140.
(45) Kunimatsu, K.; Samant, M. G.; Seki, H. In-Situ FT-IR Spectroscopic Study of Bisulfate and Sulfate Adsorption on Platinum Electrodes: Part 1. Sulfuric Acid. *J. Electroanal. Chem. Interfacial Electrochem.* **1989**, *258* (1), 163−177.
(46) Johnston, D. H.; Shriver, D. F. Vibrational Study of the Trifluoromethanesulfonate Anion: Unambiguous Assignment of the Asymmetric Stretching Modes. *Inorg. Chem.* **1993**, *32* (6), 1045−1047.
(47) Ferry, A.; Jacobsson, P.; Stevens, J. R. Studies of Ionic Interactions in Poly(Propylene Glycol)4000 Complexed with Triflate Salts. *J. Phys. Chem.* **1996**, *100* (30), 12574−12582.
(48) Bergström, P.-Å.; Lindgren, J. An Infrared Spectroscopic Study of the Hydration of the Triflate Ion (CF3SO-3) in Aqueous Solution. *J. Mol. Struct.* **1990**, *239*, 103−111.
(49) Prasanna, C. M. S.; Suthanthiraraj, S. A. Electrical, Structural, and Morphological Studies of Honeycomb-like Microporous Zinc-Ion Conducting Poly (Vinyl Chloride)/Poly (Ethyl Methacrylate) Blend-Based Polymer Electrolytes. *Ionics* **2016**, *22* (3), 389−404.
(50) Hamidi, M. E. M.; Pascal, J.-L. Synthesis and Structural Characterization of Some Anhydrous Ln(OTf)3 Complexes (Ln = Sc, La, Nd, Sm, Gd and Er; OTf = CF3SO3). *Polyhedron* **1994**, *13* (11), 1787−1792.
(51) Vatamanu, J.; Borodin, O. Ramifications of Water-in-Salt Interfacial Structure at Charged Electrodes for Electrolyte Electrochemical Stability. *J. Phys. Chem. Lett.* **2017**, *8* (18), 4362−4367.
(52) Luschtinetz, R.; Seifert, G.; Jaehne, E.; Adler, H.-J. P. Infrared Spectra of Alkylphosphonic Acid Bound to Aluminium Surfaces. *Macromol. Symp.* **2007**, *254* (1), 248−253.
(53) Kołodziejczak-Radzimska, A.; Markiewicz, E.; Jesionowski, T. Structural Characterisation of ZnO Particles Obtained by the Emulsion Precipitation Method. *J. Nanomater.* **2012**, *2012* (1), 656353.
(54) Castañeda, L. Study of Optical Properties of Zinc Oxide Nanostructures Thin Solid Films Using Spin Coating Technique: APrecursor Organic for Electronics Devices Applications. *Biomed. J. Sci. Technol. Res.* **2020**, *31* (1), DOI: 10.26717/BJSTR.2020.31.005041.
(55) Baldelli, S.; Mailhot, G.; Ross, P. N.; Somorjai, G. A. Potential-Dependent Vibrational Spectroscopy of Solvent Molecules at the Pt(111) Electrode in a Water/Acetonitrile Mixture Studied by Sum Frequency Generation. *J. Am. Chem. Soc.* **2001**, *123* (31), 7697−7702.
(56) Dereka, B.; Lewis, N. H. C.; Keim, J. H.; Snyder, S. A.; Tokmakoff, A. Characterization of Acetonitrile Isotopologues as Vibrational Probes of Electrolytes. *J. Phys. Chem. B* **2022**, *126* (1), 278−291.
(57) Ataka, K.; Yotsuyanagi, T.; Osawa, M. Potential-Dependent Reorientation of Water Molecules at an Electrode/Electrolyte Interface Studied by Surface-Enhanced Infrared Absorption Spectroscopy. *J. Phys. Chem.* **1996**, *100* (25), 10664−10672.
(58) Sayama, A.; Nihonyanagi, S.; Ohshima, Y.; Tahara, T. In Situ Observation of the Potential-Dependent Structure of an Electrolyte/Electrode Interface by Heterodyne-Detected Vibrational Sum Frequency Generation. *Phys. Chem. Chem. Phys.* **2020**, *22* (4), 2580−2589.
(59) Lahiri, A.; Borisenko, N.; Borodin, A.; Olschewski, M.; Endres, F. Characterisation of the Solid Electrolyte Interface during Lithiation/Delithiation of Germanium in an Ionic Liquid. *Phys. Chem. Chem. Phys.* **2016**, *18* (7), 5630−5637.
(60) Hoane, A. G.; Zheng, Q.; Maldonado, N. D.; Espinosa-Marzal, R. M.; Gewirth, A. A. Impact of Multivalent Cations on Interfacial Layering in Water-In-Salt Electrolytes. *ACS Appl. Energy Mater.* **2024**, *7* (12), 5179−5192.
(61) Reber, D.; Takenaka, N.; Kühnel, R.-S.; Yamada, A.; Battaglia, C. Impact of Anion Asymmetry on Local Structure and Supercooling Behavior of Water-in-Salt Electrolytes. *J. Phys. Chem. Lett.* **2020**, *11* (12), 4720−4725.
(62) Zhao, K.; Liu, F.; Fan, G.; Liu, J.; Yu, M.; Yan, Z.; Zhang, N.; Cheng, F. Stabilizing Zinc Electrodes with a Vanillin Additive in Mild Aqueous Electrolytes. *ACS Appl. Mater. Interfaces* **2021**, *13* (40), 47650−47658.
(63) Schick, B. W.; Hou, X.; Vanoppen, V.; Uhl, M.; Kruck, M.; Berg, E. J.; Jacob, T. Revealing the Structural Evolution of Electrode/Electrolyte Interphase Formation during Magnesium Plating and Stripping with Operando EQCM-D. *ChemSusChem* **2024**, *17* (4), No. e202301269.
(64) Shpigel, N.; Levi, M. D.; Aurbach, D. EQCM-D Technique for Complex Mechanical Characterization of Energy Storage Electrodes: Background and Practical Guide. *Energy Storage Mater.* **2019**, *21*, 399−413.
(65) Yang, Z.; Dixon, M. C.; Erck, R. A.; Trahey, L. Quantification of the Mass and Viscoelasticity of Interfacial Films on Tin Anodes Using EQCM-D. *ACS Appl. Mater. Interfaces* **2015**, *7* (48), 26585−26594.
(66) Leppin, C.; Peschel, A.; Meyer, F. S.; Langhoff, A.; Johannsmann, D. Kinetics of Viscoelasticity in the Electric Double Layer Following Steps in the Electrode Potential Studied by a Fast Electrochemical Quartz Crystal Microbalance (EQCM). *Analyst* **2021**, *146* (7), 2160−2171.
(67) Nguyen, H. K.; Shundo, A.; Ito, M.; Pittenger, B.; Yamamoto, S.; Tanaka, K.; Nakajima, K. Insights into Mechanical Dynamics of Nanoscale Interfaces in Epoxy Composites Using Nanorheology Atomic Force Microscopy. *ACS Appl. Mater. Interfaces* **2023**, *15* (31), 38029−38038.
(68) Sodeyama, K.; Yamada, Y.; Aikawa, K.; Yamada, A.; Tateyama, Y. Sacrificial Anion Reduction Mechanism for Electrochemical Stability Improvement in Highly Concentrated Li-Salt Electrolyte. *J. Phys. Chem. C* **2014**, *118* (26), 14091−14097.
(69) Khan, Z.; Kumar, D.; Crispin, X. Does Water-in-Salt Electrolyte Subdue Issues of Zn Batteries? *Adv. Mater.* **2023**, *35* (36), 2300369.
(70) Qiu, H.; Du, X.; Zhao, J.; Wang, Y.; Ju, J.; Chen, Z.; Hu, Z.; Yan, D.; Zhou, X.; Cui, G. Zinc Anode-Compatible in-Situ Solid Electrolyte Interphase via Cation Solvation Modulation. *Nat. Commun.* **2019**, *10* (1), 5374.


https://doi.org/10.1021/acsami.4c15318
ACS Appl. Mater. Interfaces XXXX, XXX, XXX−XXX